Joint measurement of the atmospheric muon flux through the Puy de Dôme volcano with plastic scintillators and Resistive Plate Chambers detectors

F. Ambrosino, A. Anastasio, A. Bross, S. Béné, P. Boivin, L. Bonechi, C. Cârloganu, R. Ciaranfi, L. Cimmino, C. Combaret, et al.

FERMILAB-PUB-15-653-APC-PPD
ACCEPTED

Joint measurement of the atmospheric muon flux through the Puy de Dôme volcano with plastic scintillators and Resistive Plate Chambers detectors

F. Ambrosino,[1,2] A. Anastasio,[2] A. Bross,[3] S. Béné,[4] P. Boivin,[5] L. Bonechi,[6] C. Cârloganu,[4] R. Ciaranfi,[7] L. Cimmino,[1,2] Ch. Combaret,[8] R. D'Alessandro,[6,7] S. Durand,[9] F. Fehr,[4] V. Français,[4] F. Garufi,[1,2] L. Gailler,[5] Ph. Labazuy,[5] I. Laktineh,[8] J-F Lénat,[5] V. Masone,[2] D. Miallier,[4] L. Mirabito,[8] L. Morel,[9] N. Mori,[6,7] V. Niess,[4] P. Noli,[2] A. Pla-Dalmau,[3] A. Portal,[5] P. Rubinov,[3] G. Saracino,[1,2] E. Scarlini,[6,7] P. Strolin,[1,2] B. Vulpescu[4]

Corresponding author: C. Cârloganu (Cristina.Carloganu@in2p3.fr), P. Noli (noli@na.infn.it)

[1]Dipartimento di Fisica,Università degli

Operated by Fermi Research Alliance, LLC under Contract No. DE-AC02-07CH11359 with the United States Department of Energy.

Abstract. The muographic imaging of volcanoes relies on the measured transmittance of the atmospheric-muon flux through the target. An important bias affecting the result comes from background contamination mimicking a higher transmittance. The MU-RAY and TOMUVOL collaborations measured independently in 2013 the atmospheric muon flux transmitted through the Puy de Dôme volcano using their early prototype detectors, based on plastic scintillators and on Glass Resistive Plate Chambers, respectively. These detectors had three (MU-RAY) or four (TOMUVOL) detection layers of 1 m^2 each, tens (MU-RAY) or hundreds (TOMUVOL) of ns time resolution, a few mm position resolution, an energy threshold of few hundreds MeV and no particle identification capabilities. The prototypes were deployed about 1.3 km away from the summit, where they measured, behind rock depths larger than 1000 m, remnant fluxes of $1.83\pm0.50(\text{syst})\pm0.07(\text{stat})$ $m^{-2}day^{-1}deg^{-2}$ (MU-RAY) and $1.95\pm0.16(\text{syst})\pm0.05(\text{stat})$ $m^{-2}day^{-1}deg^{-2}$ (TOMUVOL), that roughly correspond to the expected flux of high-energy atmospheric muons crossing 600 metres water equivalent (m.w.e) at 18° elevation. This implies that imaging depths larger than 500 m.w.e from 1 km away using such prototype detectors suffers from an overwhelming background. These measurements confirm that a new generation of detectors with higher momentum threshold, time-of-flight measurement and/or particle identification is needed. The MU-RAY and TOMUVOL collaborations expect shortly

Studi di Napoli Federico II, Italy.

to operate improved detectors, suitable for a robust muographic-imaging of kilometre scale volcanoes.

---

[2]INFN, Napoli, Italy.

1. Muon imaging of volcanoes

[3]Fermilab PO Box 500 Batavia IL 60510-5011

[4]Clermont Université, Université Blaise Pascal, CNRS/IN2P3, Laboratoire de Physique Corpusculaire, BP 10118, F-63000 Clermont-Ferrand, France.

[5]Laboratoire Magmas et Volcans, Université Blaise Pascal - CNRS - IRD, OPGC, 5 rue Kessler, 63038 Clermont Ferrand, France.

[6]Dipartimento di Fisica,Università degli Studi di Firenze, Italy.

[7]INFN, Firenze, Italy.

[8]Université de Lyon, Université Lyon 1, CNRS/IN2P3, IPNL, 1 Rue E. Fermi, 69622 Villeurbanne Cedex, France.

[9]Ecole Supérieure des Géomètres et Topographes du Mans, France.

Volcanic hazard assesment and risk mitigation remain two very important scientific subjects with heavy implications both on the population safety and economic development [*Brown et al.*, 2015]. Anticipating future activity of volcanoes requires monitoring of their activity as well as information on their past behaviour and their internal structure. Monitoring volcano activity, that may be regarded as dynamic imaging of changes occurring inside and below the edifices, routinely uses a large number of methods (see for example [*Smith*, 2009]). Structural geophysical studies, that may be considered as static imaging, aim at identifying and characterising the architecture of the edifices, their plumbing systems, as well as the mechanical characteristics of the rocks. They are inferred from the internal distribution of various physical quantities such as electrical resistivity [*Revil*, 2008], density [*Li*, 1998; *Gailler*, 2009], magnetisation [*Gailler*, 2012], or seismic velocity [*Lees*, 2007]).

The plumbing system comprises magma reservoirs and conduits. Magma reservoirs are usually located at depths ranging from few to tens of kilometres and therefore may be detected only by techniques with a large depth of investigation. The conduits connect magma reservoirs to the surface. More superficial than the reservoirs, their size is also smaller than typical reservoir sizes, which may increase the detection difficulty. Typical sizes vary from metres in case of the mafic dikes to hundreds of metres for the chimney of more felsic magmas. The architecture of the edifices is important to know because it will not only influence the magma paths (the conduits), but it may also generate its own volcano-tectonic activity through gravitational instabilities [*Mc Guire*, 1996]. For example, zones of an edifice weakened by hydrothermal alteration will be prone to slide as huge flank landslides [*Siebert*, 1987; *Lopez and Williams*, 1993].

The need of high resolution imaging of the interior of the volcanic edifices is therefore well justified and is a main motivation for developping and refining the geophysical methods currently employed in volcanology.

Recently, radiography with atmospheric muons [*Alvarez*, 1970; *Nagamine*, 1995], referred to as muography in the following, was made possible by the development of reasonably priced, large area, high efficiency and high precision muon trackers. Several groups ([*Tanaka*, 2007, 2010, 2011; *Marteau*, 2012; *Lesparre*, 2012; *Fehr*, 2012; *Portal*, 2013; *Tanaka*, 2014]) have already applied this method for the exploration of volcanic edifices of moderate size.

The basic idea behind volcano muography is that measuring the absorption of the atmospheric muon flux as a function of the direction at a fixed location allows mapping out the average column density in the volcano after accounting for the topography. By repeating the measurement from different locations, three-dimensional models of the matter density distribution can be inferred.

Muography offers some clear advantages over traditional geophysical methods in terms of attainable resolution and ease of installation and deployment since the measurement can be performed remotely from the risk area whereas most other geophysical methods require to make measurements on the field above the active areas. The muography suffers though from the fact that the high energy muons that can cross large edifices are rare. This has a direct implication on the size of the detectors that need to be deployed in order to measure a sizeable number of events in a reasonable time. It also requires a very tight control of the background affecting the measurements, be it physical or detector induced.

In this contribution, we describe a new muography experiment on a complex volcanic edifice, a compound lava dome. Lava domes are volcanic edifices created both by magma intrusion into the dome interior (endogenous growth) and by extrusion of spines, lobes or short lava flows (exogenous growth). Dome magmas are too viscous to flow over significant distances and will accumulate above and near the vent. Domes exhibit a large range of shapes and sizes, depending on their construction history. Their surface is often constituted by rock fragments forming a talus on the sides. Inside, cores of solidified magma are present. Domes seldom form during a single episode. Most of the time successive episodes of dome growth occur during an eruption of highly variable duration, that can last weeks or years. Collapse of parts of the dome may be accompanied by explosions and pyroclastic flows. The compound lava dome formed by the end of the eruption includes volcanic ash and pyroclastites intermixed with rock fragments derived from solidified lava and massive intrusions and extrusions. Its flank will be composed of unstable rock debris.

Such complex formations of compound lava domes have been well documented in recent eruptions of Mount Saint Helens [*Major*, 2009; *Vallance*, 2010; *Swanson*, 1987], Unzen [*Nakada*, 1993, 1995, 1999], Montserrat [*Calder*, 2002; *Ryan*, 2010; *Watts*, 2002] or Santiaguito [*Bluth*, 2004; *Harris*, 2003; *Rose*, 1972]. When the formation of a compound dome has not been witnessed or monitored, its history and internal structure are more difficult to establish. They will rely on geological analysis of the products at the surface and on structural geophysical studies. Moreover, even in the case of compound lava domes monitored during growth, the internal structure may be poorly known since internal processes as endogenous growth or hydrothermal activity cannot be observed directly.

The compound lava dome of the experiment is the Puy de Dôme, located in the Chaîne de Puys volcanic district in France. This ∼11000 years old edifice has an altitude of 1465 m (a.s.l) and a lateral extension of more than 2 km at the base. Geological studies lead to a three-step model for the Puy de Dôme growth [*Boivin*, 2009; *Camus*, 1975]. A first cumulo-dome, emplaced on a cluster of several scoria cones and their associated lava flows, forms the western part of the volcano. After the partial destruction of the eastern part of this unit, a spiny extrusion grew into the collapse scar, forming the second unit. The eruption ended by a summit phreatic/phreatomagmatic event [*Miallier*, 2010]. The alteration observed on several summit outcrops indicates that the growth of Puy de Dôme was accompagnied by a strong fumarolic and hydrothermal activity.

The Puy de Dôme is an interesting target for muon imaging. It is isolated and its basement at an altitude of about 950 m (a.s.l) greatly facilitates the deployment of muon detectors. The edifice size is moderate enough to expect that a large part may be investigated with atmospheric muons. The recent geology survey [*Boivin*, 2013] and a preliminary geophysical survey [*Portal*, 2013] raise questions over the validity of the previous model and suggest that the interior of the edifice is heterogeneous. This geological heterogeneity should be reflected in the density distribution.

This first attempt by the MU-RAY [*Ambrosino*, 2014; *Anastasio*, 2013; *Anastasio, bis*, 2013; *Ambrosi*, 2011] and TOMUVOL [*Cârloganu*, 2013] collaborations to measure through muography the transmittance of the inner structure of the Puy de Dôme was made in 2013.

The two detectors, described in detail in Section 2 and Section 3, are modular, robust and designed for low power consumption, despite a fine segmentation and three or four

tracking layers. They differ in the detection techniques and the two collaborations have used independent data acquisition and analysis strategies. They are both prototypes of more advanced detectors foreseen for the muography, that will have higher momentum thresholds and will include time-of-flight measurements.

Since muography is a new technique and the robustness of the density measurement versus experimental and methodological biases was not assessed yet, we have chosen to treat the Puy de Dôme measurement reported here as two independent experiments performed with the two detectors, rather than a combined one. This approach is conservative and should lead to the identification of eventual detection biases, specific for each of the two detectors. Similarly, the methodological part (detector calibration, muon reconstruction and selection of the muon candidates used for inferring the target transmittance) is also independent and should allow us to infer the systematical biases affecting the muographic measurements from the difference between the MU-RAY and TOMUVOL results.

One of the major advantages of the muography being the capability of performing measurements from the outskirts of the risk areas, the two detectors were deployed about 1.3 km away from the summit, at about the same altitude (1000 m a.s.l). The detection views were South-North for the MU-RAY detector and East-West for the TOMUVOL detector as it can be seen on the top picture of Figure 1. We use a detector-wise elevation (α) - azimuth (β) coordinate system rotated about the vertical axis such that azimuth zero is the normal to the first detection layer pointing towards Puy de Dôme. It was checked that the detection layers were vertical with an accuracy better than 1 degree. In this right-handed coordinate system with the origin set in turn by each detector, the path

length that the atmospheric muons would have to travel through the volcano in order to reach the detectors is represented in the middle and bottom plots of Figure 1.

The path lengths were calculated from a high resolution digital elevation model re-binned using $2.5 \times 2.5 \times 2.5$ m^3 bins.

Two regions in α and β with path lengths in the 1.5 to 2 km range, called in the following "control regions", are defined for each site. They are represented by black rectangles superimposed on the path length plots of Figure 1.

To estimate the number of expected muon events crossing the volcano in a given direction, the two collaborations use two different strategies. MU-RAY follows the method described in [*Okubo*, 2012]: first, the atmospheric muon flux (differential in energy and zenith angle), is evaluated using the Matsuno model as reported in [*Matsuno*, 1984]; then a transmission table giving the percentage of surviving muons as a function of the integrated density of rock to cross is calculated using the GEANT4 simulation toolkit [*GEANT4*, 2003], in which the majority of the physics processes involving high energy muons are simulated; after estimating along each direction the rock thickness, the flux is convoluted with the transmission to infer the expected number of events for each direction.

TOMUVOL uses the differential spectrum of atmospheric muons from [*Chirkin*, 2004]. In the model proposed therein, the altitude correction is implemented for the average track length of the muons and for the atmosphere mass overburden using the exponential atmospheric model, as cited in the paper. Neglecting the scattering, high energy muons are then assumed to follow straight-line trajectories from their generation point in the upper atmosphere down to sea level. The energy loss of muons in the matter crossed during their travel is computed with the Continuously Slowing Down Approximation

(CSDA) [*Groom*, 2001], using the tabulated values for "dry air" and "standard rock" (with a density renormalised to 1.66 g/cm^3) as provided online by [*PDG*, 2014].

The value of 1.66 g/cm^3 was suggested by density measurements of about 100 rock samples collected on various parts of the Puy de Dôme. The sample densities range between 1.2 and 2.15 g/cm^3. It is unlikely that densities significantly higher than 2.15 g/cm^3 exist in the bulk of the dome because the measured samples should represent all the known structural units of the volcano. Actually, the batch mean-value is 1.88 g/cm^3, but the relative contributions of the different petrographic facies in the batch are certainly not the same as for the whole edifice. Moreover, the mean density at a multi-metric scale should account for voids between rocky materials, for example within cracks or loose deposits. Also, the Nettleton test on the gravimetry measurements [*Portal*, 2013] finds that the Bouguer anomalies are least correlated with the altitude when assuming an average density of the dome of 1.8 g/cm^3. Let us stress though that the average density of the dome is used here just for having a first order estimate of the expected number of muons crossing the volcano. The actual density measurement (Section 4) does not require a first guess of the volcano average bulk density as in the case of the gravimetric tomography. The ballistic muons crossing the volcano along a given direction are independent of the ballistic muons crossing along other directions and thus are the measurements of the integrated densities along different directions, provided that the flux of atmospheric muons is correctly accounted for.

The TOMUVOL approach was used to estimate the number of muons originating from the control regions defined in Figure 1, that should be recorded with an ideal detector of size 1 m×1 m×1 m, when located in turn at the two deployment sites and pointing

towards ($\alpha = 0, \beta = 0$). The expected statistics after one month of data taking is shown in Figure 2. The muon rate is estimated to be 30 μHz for the MU-RAY deployment site and 14 μHz for the TOMUVOL site. The MU-RAY approach leads to an estimate of 56 μHz for the MU-RAY site. Although the expected rates using the two approaches differ by nearly a factor two, this (as will be shown in section 4) pales into insignificance when compared to the actual measured rates.

For completeness sake, let us quote also the muon rates in an ideal, 1 m$\times$1 m$\times$1 m detector located at the MU-RAY site, following the MU-RAY approach and assuming extreme densities of 1 and 2.5 g/cm^3. They are of 267 μHz and 10 μHz respectively.

In fact, for realistic densities, it is obvious that in the control regions at the very base of the Puy de Dôme, there is a small expectation of detecting high energy muons crossing the volcano with a 1 m$\times$1 m$\times$1 m detector during one month of data taking. These regions can therefore be used as control regions for the background affecting the measurement. It should be stated that the regions are shifted by 4° from the horizontal, since none of the two detectors had for this campaign a time-of-flight measurement; both are therefore unable to discriminate between the tracks arriving from the volcano side and from the opposite side when the tracks are nearly horizontal. However, as it will be seen in the following sections, the angular resolutions of both detectors are good enough that above $\alpha \sim 4°$ the residual contamination with tracks from the opposite direction should be negligible. Technical developments are underway within both collaborations and in the future both detectors are expected to have a time-of-flight measurement.

After reporting on the measurements of the muon flux in the free sky and through the Puy de Dôme performed independently by the MU-RAY and TOMUVOL collaborations

in Section 4, the implication on the muography of kilometre scale volcanoes is discussed in Section 5.

2. The MU-RAY detector

The MU-RAY telescope [*Anastasio*, 2013] is based on plastic scintillators. Each scintillator bar has a triangular cross-section, with a base of 3.3 cm, a height of 1.7 cm and a length of 107 cm. The bars, produced at FERMILAB-NICADD [*Pla-Dalmau*, 1999], are extruded and coated with a TiO_2 layer 0.25 mm thick to increase the light yield. A hole along the bar axis hosts a Wave Length Shifting (WLS) fibre. A module of 32 bars grouped together is 0.5 m wide and weighs less than 20 kg. The 32 fibres are routed to a specifically designed fibre connector that is coupled to a custom designed Printed Circuit Board (PCB). The PCB board hosts 32 silicon photomultipliers (SiPMs), custom designed by FBK-IRST [*Piazza*, 2010].

When a muon crosses a scintillator bar, light is produced. The WLS fibres collect and carry the light to the SiPMs, which convert the light pulse into an electric signal, processed by the front end electronics (Slave board). The Slave outputs a fast digital signal whenever one or more SiPM produce a signal above a programmable threshold (local trigger). The local trigger is carried to a control board (Master), which collects all the local triggers that have been sent from the Slave modules and produces a global trigger signal according to a programmable trigger logic. The charge produced by each SiPM is proportional to the energy released by the muon in the scintillator bar and is converted by an Analog to Digital Converter (ADC) and acquired by the Master board.

Two modules, assembled side by side, form an X or Y layer of about 1 m^2 area, giving one of the two "cartesian" coordinates of the impact point of the muon on the layer. Two

layers with orthogonal bars form an X-Y plane. The telescope consists of three X-Y layers, mounted on an aluminium alloy frame. The frame can be rotated in the azimuthal plane, to acquire data with the telescope pointing to different regions of the sky for calibration purposes. The muon trajectory is reconstructed by a linear fit of the X-Y-Z points given by the three layers.

The SiPMs have a very low power consumption, are robust and compact. Their main drawback is the temperature dependence of the operating voltage and the high dark rates (compared to conventional phototubes), due to the thermally produced electron-hole pairs. In order to maintain the temperature under control, the SiPMs are thermally coupled through their PCB carrier to an external source kept at constant temperature. The specially developed water cooling system gives a temperature stability better than 0.1°C.

The dark rates of the SiPMs used for the measurement presented here were as high as 1-2 MHz, though SiPMs with a lower dark rate are foreseen in the future. The discriminator threshold of the Slave was set such as to have, on average, a trigger rate of less than 2 kHz per SiPM, equivalent to about a 100 kHz rate per single view (X or Y) . The local trigger signal has a width of 40 ns. The trigger logic is the coincidence of the six single view planes. The expected rate of random coincidences and the rate measured in the laboratory (less than 1 event per day) are far below the expected muon rate.

When a global trigger is produced, the Master board starts the data acquisition (DAQ) from the 12 Slaves. The maximum DAQ rate is 20 Hz. During the measurement campaign the measured trigger rate was of the order of few Hz and the typical correction for the dead time of the order of 20%.

An iron shield of 1 m^2 area and 3 cm thickness was installed between the first and the second X-Y plane along the muon direction to stop muons with energy below 70 MeV and part of the cosmic soft component, i.e. electrons and positrons.

2.1. The Puy de Dôme measurement campaign

The MU-RAY detector has been deployed on the Puy de Dôme from beginning of June 2013 to the beginning of December 2013. Data recording was discontinued from July 22 till September 5 because of a storm, that damaged the commercial internet network for the remote control of the telescope. Apart from this, recording was successful for a total of 105 days. The first 4 and the last 9 days were devoted to calibration runs, with the telescope pointing towards the free sky. Data recording with the telescope pointing towards the Puy de Dôme lasted 92 days in total.

Each single data recording run consisted of 10^4 triggers and on average lasted about 45 minutes. Before each run, 10^4 pedestal events were acquired. The local trigger rates of each board, which are dominated by dark count rates, were also measured. All these activities reduce the effective time, devoted to the physics data run, to about 87% of the total run time. The trigger logic required a signal from at least one of the scintillator bars belonging to each of the six X or Y planes. A small percentage ($\sim 0.1\%$) of the triggered events contained corrupted data and were discarded during data analysis.

During the data taking period the trigger rate was stable, with an average value of 3.59 ± 0.29 Hz.

2.2. Data reconstruction and analysis

The data analysis starts with the reconstruction of the muon tracks event by event. The track reconstruction is performed independently in the X-Z and Y-Z projections, where X, Y and Z respectively give the horizontal, vertical and longitudinal coordinates.

A normalised energy is associated to each strip, defined as the ratio of the difference between the recorded ADC value and the mean pedestal value, respect to the r.m.s value of the pedestal distribution. Strip clusters are formed by grouping one or more neighbouring strips with a normalised energy greater than 5. To each cluster is associated a normalised energy and a position defined respectively as the sum of the strips energies and as the energy weighted average of the strips coordinates. Therefore the clusters give the X-Z or Y-Z coordinates of a muon or any other particle that released enough energy in the strips.

Each cluster in the first plane is associated with a cluster in the third plane and the intersection of the straight line connecting the two clusters with the middle plane is evaluated. If a cluster is found in its neighbourhood, a linear fit of the three clusters is performed and, if the fit converges, a candidate track in a single view is defined.

The procedure is repeated for all cluster combinations and produces a list of candidate tracks in both the X-Z and Y-Z projections. For each projection, the track candidate with the highest value of the minimum cluster energy is defined as the best candidate track. The three dimensional best candidate track is given by the two best candidate tracks in the two projections. In this procedure all the cuts are loose enough to ensure a high reconstruction efficiency. 92% of the events have at least one candidate track in each view.

To increase the quality of the tracks some further cuts are introduced (quality cut). The $\chi^2/n.d.f.$ of the fit must be less than 5 and the minimum energy of the cluster associated to the track must be greater than 20.

The maximum $\chi^2/n.d.f.$ value and the minimum energy of the cluster were obtained from a multi-parameter minimisation of the Punzi estimator [*Punzi*, 2003]. The procedure maximises the efficiency of the selection for the muons sample while minimising the acceptance for random triggers.

In this sample we select events containing just a single muon track (golden tracks) by using an isolation cut. This cut is intended to reject events with tracks generated by the soft component of the cosmic ray. The soft component can produce a shower hitting the detector, generating more than one track or one track and one or more physical clusters. The isolation cut requires that no cluster having a normalised energy greater than 20 and not associated to the best candidate track is present in the event and that the number of strips forming the clusters associated to the best track is less than 5. This golden tracks sample has a track fit residual distribution with a standard deviation of ~ 4 mm.

We define the selection efficiency $\epsilon_{sel}(\alpha, \beta)$ as the number of events that satisfy, for each view, the isolation cut divided by the number of events selected with the previous cuts. In Figure 3 $\epsilon_{sel}(\alpha, \beta)$ is shown for both the forward and backward track directions. At the end of this selection we estimate an average analysis efficiency $\epsilon_{ana} = 47\%$.

The golden track rate, of 1.99 ± 0.12 Hz is shown in Figure 4 as a function of time. The background rate, defined as the rate of tracks pointing towards the control region defined in Section 1, was measured to be 0.7 ± 0.1 mHz and is also represented as a function of time by open red squares. It must be noticed that neither rates are correlated

to the temperature of the SiPMs though the local trigger rates are clearly correlated with their temperature. During the whole data taking period $\sim 11.4 \times 10^6$ golden tracks were acquired. The ones pointing in the direction of Puy de Dôme are shown on Figure 5 as a function of the elevation angle α and azimuth β.

The stripes that can be noticed in the Figure 5 are due to the discrete resolution of the detector. The impact position of a track is not continuous, but varies in steps being calculated from the position of the scintillators bars centres. As a consequence, α and β exhibit also discrete distributions.

3. The TOMUVOL detector

The TOMUVOL muon telescope is made of four parallel layers of gaseous trackers, Glass Resistive Plate Chambers (GRPCs) [*Bedjidian*, 2011] originating from research and development for the International Linear Collider detectors [*ILC*, 2013]. A single GRPC consists of two parallel thin glass plates kept 1.2 mm apart by tiny spacers so that gas (a mixture of TFE, SF6 and isobutane) can circulate between the plates. The outer sides of the glass plates are coated with a thin layer of resistive material on which high voltage is applied. Charged particles, passing through the chambers, ionise the gas and thus produce charge cascades, which in turn induce charge signals on 1 cm^2 copper cells etched on one face of a PCB placed on the anode glass. On the other face of the PCB are attached the readout ASICs, named Hardroc2 [*Callier*, 2014; *Seguin-Moreau*, 2009]. The ASICs dispose of three independent comparators that provide amplitude information about the registered signals; they also timestamp the signals using a 5 MHz clock. The GRPCs are operated in avalanche mode, with the high voltage (typically 7 kV) being adapted

continuously to environmental pressure and temperature conditions in order to ensure a stable working point both in terms of detection efficiency and dark noise.

The chambers and their readout electronics are placed in aluminium cassettes for protection while also simplifying greatly the handling of the detector: they are 361×746 mm^2 large, 31 mm thick, weigh 6 kg each and are transported in a standard foam packaging. Each detection layer, about 1 m^2 large, consists of 6 cassettes inserted in a light aluminium structure. The separation between the layers is 33 cm, amounting to a total lateral extension of the telescope of 1 m. Low and high voltage are distributed to transfer boxes attached to each layer and further routed to the detector through cabling internal to the aluminium frame. Similarly, the gas distribution is chained through the individual chambers with a unique inlet and outlet per layer. This way, mounting and dismounting of the detector is greatly simplified.

A dedicated board on each detection unit, the DIF [*Adloff*, 2013], using Field Programmable Gate Arrays (FPGAs) serves as an interface between its PCB and the master clock on one side and the acquisition computer on the other side. The synopsis of the data acquisition is as follows: each ASIC reads out 64 pads and stores up to 128 events (an event is at least one signal in one of the 64 pads read by the ASIC with an amplitude above a predefined threshold) in its internal memory. Once an ASIC fills its memory it sends out a readout request; the DIF board listens continuously for readout requests originating from the 24 ASICs on its attached detector unit and forwards the requests to the master clock board. When the master clock receives a readout request from one of the 24 DIFs of the detector, it stops the acquisition and triggers the readout of the entire detector, in parallel for all the DIFs and serialised to the detector unit level. After

the data from the memory of the last ASIC in the chain are read out, the master clock enables again the data acquisition and the cycle repeats.

To operate the DAQ system, a conventional computer is used to send the commands to the master clock board and to collect the data from the 24 detection units. The low dark noise rate ($\sim$0.3 Hz/cm^2) allows for a full readout of the chambers, without imposing coincident signals among chambers situated in different layers. It is possible to filter the data on the acquisition computer such that only coincident hits in two or three of the four layers are kept. Conversely, if necessary for detailed detector studies, the entire data can be recorded.

3.1. The Puy de Dôme measurement campaign

From beginning of November 2013 to middle of January 2014, the TOMUVOL detector was deployed in a ground-level building with a very light metallic structure. It was powered from a standard electrical outlet and remotely controlled using a small radio-antenna transmitting the data to a powerful antenna situated at the summit of the volcano operated by the Puy de Dôme Observatory [*OPGC*].

The total data taking duration was of 41 days, out of which 7 days were dedicated in the beginning to detector calibration. The data taking was stopped from December 25th to January 8th. During the data taking the efficiency of individual GRPCs has been estimated on a per run basis, a run being arbitrarily chosen to last 12h. Similarly the detection dead time (the time duration when the GRPCs are read out and hence tracks passing through them are not recorded) is measured on a per run basis, though stability checks were performed frequently during the run. Overall, the mean value of the chamber

detection efficiency over the 24 GRPCs was of $\sim 95\%$. The dead time during the stable runs was 6.0 ± 1.1 %, with an average value of 7 % over the whole data taking period.

The track reconstruction uses only events with coincident hits in all four layers of the detector. The measured coincidence rate was 3.5 ± 0.1 Hz.

3.2. Data reconstruction

The reconstruction algorithm preselects coincident hits in a 200 ns time window in at least three of the four detection layers, from which tracks are obtained analytically through a straight line minimisation procedure, which allows for track bundles. The overall χ^2-distribution of the track residuals agrees well with the expectation both in the case of 3-layer tracks (χ^2 distribution with two degrees of freedom) and of 4-layer tracks (χ^2 with four degrees of freedom). In the following, the 3-layer and the 4-layer tracks with $\chi^2/ndf \leq 5$ are called "reconstructed tracks". Even though only the high quality 4-layer tracks are used in the analysis, the 3-layer tracks allow us to monitor in real time the efficiency of the GRPCs and the overall acceptance. Among the 4-layer tracks, only fully isolated tracks, i.e. without any signal recorded in the detector that cannot be directly linked to the track, are selected.

The background, as defined in Section 1, is further reduced in the final sample with respect to the well reconstructed tracks by requiring the tracks to have a $\chi^2/n.d.f \leq 0.8$. This tight $\chi^2/n.d.f$ selection is imposed by the optimisation of the measurement sensitivity that in turn requires minimising the background flux.

It is interesting to notice in Figure 6 that if the selection efficiency, defined as the ratio between the number of selected tracks and the number of 4-layer, reconstructed tracks, is almost 65 % for the free sky tracks, it drops to 30 % in the case of the tracks pointing

towards Puy de Dôme. This hints at a significant difference in the population of tracks pointing towards the volcano and towards the free sky, respectively.

As in the case of the MU-RAY collaboration, the selected tracks are called in the following "golden tracks" and their rate as a function of time over the whole data taking period is shown in Figure 7. The measured mean value is 1.64 ± 0.08 Hz. A total of 4.95 million of golden tracks were registered, out of which 1.45 million served for cross-checks and 3.5 million were used in the analysis. The background rate is also stable over the 34 days of data taking with a mean of 0.93 ± 0.11 mHz, that is more than a factor of 60 larger than the expected signal from high energy muons crossing the control region.

The golden tracks sample shows X and Y residuals with means close to 0 and a standard deviation better than 1.5 mm, proving that the chambers were sufficiently aligned by construction, without any additional measurements on site.

The full statistics of golden tracks pointing towards the Puy de Dôme is represented in Figure 8 as a function of the elevation angle α and azimuth β. The volcano topographical shape is superimposed in black and it is in an excellent agreement with the volcano shadow, as inferred from the depletion in the number of muons.

4. Muon flux measurement

4.1. Methodology

A useful quantity for characterising the behaviour of a detector meant for measuring a flux of particles is the effective surface, S_{eff}, which takes into account the detection performance (ϵ) and the geometrical acceptance of the detection setup ($\mathcal{A}$). The detection performance $\epsilon(\alpha, \beta, p)$ includes the changes in detection, reconstruction and selection efficiency with the momentum p of the incoming particle and its direction of incidence on

the detector, given by the angles α and β:

$$\mathcal{S}_{eff}(\alpha,\beta,p) = S_{detector} \cdot \mathcal{A}(\alpha,\beta) \cdot \epsilon(\alpha,\beta,p) \quad (1)$$

Only the detector area orthogonal to the incident direction of the particle is effective for the detection. Moreover, in the case of the muon telescopes made of parallel layers of finite dimensions, the particles are required to physically cross the outer layers in order to induce coincident signals. This factor, generally known in the literature as geometrical acceptance or geometrical factor, can be analytically calculated for a perfect telescope with square layers of size l^2 and a distance d between the two outermost layers as

$$\mathcal{A}(\alpha,\beta) = \cos\alpha \cdot \cos\beta \cdot \sup\left(0, 1 - \frac{d \cdot abs(\tan\beta)}{l}\right) \cdot \sup\left(0, 1 - \frac{d \cdot abs(\tan\alpha)}{l\cos\beta}\right)$$

with $sup(0,x)$ being x for positive x, 0 otherwise. In practice, the behaviour of the instrument will deviate from the ideal form due to missing or inactive detector parts, but they are easily accounted for using ray-tracing simulations.

For a telescope of known effective surface, the number of expected muons as a function of the acquisition time can be directly evaluated by convoluting the effective surface with the differential muon flux $\Phi(\alpha,\beta,p)$ expected along the direction (α,β):

$$\mathcal{N}(\alpha,\beta) = \Delta T \cdot \int_{p_{th}}^{\infty} \mathcal{S}_{eff}(\alpha,\beta,p) \cdot \Phi(\alpha,\beta,p) dp \quad (2)$$

Here, p_{th} is the detection threshold on the muon momentum and ΔT the acquisition time.

The effective surfaces estimated for the two detectors are presented in the following under the assumption that $\epsilon(\alpha,\beta,p)$ is discrete: zero below the momentum threshold and independent of the muon momentum above. It is a reasonable assumption when

taking into account the amount of matter present in the two detectors that should set the threshold in the hundreds of MeV/c - 1 GeV/c range.

The scintillators on which the MU-RAY detector is based are stable in time.

MU-RAY estimated therefore an average trigger efficiency ϵ_{trig} equal to 80% and efficiency due to the acquisition dead-time ϵ_{dt} equal to 80% from measurements performed in laboratory before the data taking campaign.

The final efficiency $\epsilon(\alpha, \beta)$ of Equation 1 can be estimated from the average efficiency due to the analysis cuts, the trigger efficiency and the dead-time efficiency:

$$\epsilon(\alpha, \beta) = \epsilon_{ana} \cdot \epsilon_{trig} \cdot \epsilon_{dt} = 0.3 \tag{3}$$

The relative uncertainty for $\epsilon(\alpha, \beta)$ is estimated to be about 10%.

In the case of the TOMUVOL detector (Figure 9, bottom), all factors affecting the effective surface are estimated continuously during data taking, using the registered data. Though the acquisition dead time is measured per run basis, the detector stability is such that the efficiencies of the individual detector cells were averaged over the whole period of data taking. Each cell efficiency is estimated as the ratio of the number of 4-layer tracks that gave a signal in that cell to the total number of tracks (be them 3-layer or 4-layer) that intersect the cell, then a toy Monte-Carlo simulation is employed to compute the effective surface of detection for golden tracks for any incoming direction. The statistical error is kept below 0.1% such that the systematics dominate the uncertainties. The total relative accuracy on the effective surface is estimated to be better than 7% which is sufficient for the present purpose. It allows us to correct for crude inhomogeneities in the golden tracks rate arising from detector inhomogeneities.

4.2. Results

The muon flux as a function of the elevation angle α and azimuth β is estimated for both MU-RAY and TOMUVOL by dividing the number of golden tracks in each 1×1 deg^2 angular bin centred on (α_i, β_i) to $\mathcal{S}_{eff}(\alpha_i, \beta_i)$. The measured flux, averaged over the azimuth bins in the control regions ($\beta \in (-4°, 16°)$ for MU-RAY and $\beta \in (-10°, 10°)$ for TOMUVOL) is represented as a function of the elevation angle α in Figure 10. The expectation assuming a uniform density for the Puy de Dôme between 1 and 2 g/cm^3 is also shown as a function of α, again averaged over $\beta \in (-4°, 16°)$.

Other than the target density, the computation of the transmitted muon flux relies on two additional free parameters: the momentum threshold, $p_{\min}$, and a global normalisation, A. Both have been fitted to the backward experimental flux over the elevation range $\alpha \in (-30°, -5°)$ and yielded the best fit values $p_{\min}$=100 MeV (for both experiments) and A = 1.270±0.228 (A=1.084±0.055) for MURAY (TOMUVOL). This means that MU-RAY measures a free-sky flux 18% lower than TOMUVOL, but both are within one standard deviation from the expectation. In the forward region, however, one clearly sees that the measured flux of golden tracks is higher, by 1 to 2 orders of magnitude, than the expected muon flux of transmitted high energy muons.

Over the fit region, the standard deviation between the best fit flux model and experimental data is within 8% for TOMUVOL and 27% for MURAY. It arises both from systematical uncertainties in the detector effective surface estimate and the flux model. We use this standard deviation as a global estimate of the systematic uncertainties affecting the remnant fluxes behind rock depths larger than 1000 m:

$$\Phi_{\mathrm{MU-RAY}} = 1.83 \pm 0.50(syst) \pm 0.07(stat) \mathrm{m}^{-2}\mathrm{day}^{-1}\mathrm{deg}^{-2} \quad (4)$$

$$\Phi_{\mathrm{TOMUVOL}} = 1.95 \pm 0.16(syst) \pm 0.05(stat) \mathrm{m}^{-2}\mathrm{day}^{-1}\mathrm{deg}^{-2} \quad (5)$$

These values roughly correspond to the expected flux of high-energy atmospheric muons at 18° elevation, crossing 600 m.w.e (or 240 m of rock with a density of 2.5 g/cm^3).

The flux measurement presented in Figure 10 shows an excellent performance of both detectors in situ: they measure accurately the expected direct flux of charged particles from the atmosphere. The atmospheric muons are largely dominating among these charged particles, and consequently this is de facto a measurement of the atmospheric muon flux, though simple trackers as ours cannot distinguish the nature of the incoming particles or measure their momentum.

The situation becomes more complex when measuring the remnant flux behind a volcano, i.e. the forward region at positive elevations in Figure 10. The soft component of the charged-particles spectrum is little to none affected by the presence of the volcano since such particles do not traverse the volcano. They arrive on the detector scattered from the free sky, since lower the momentum of the particle, larger its scattering is while propagating. The high energy, ballistic muons that cross the volcano and whose transmittance caries the density information, are however greatly diminished by the absorption in the rock. As an order of magnitude example, the expected flux in the free sky at an elevation of 24° drops by a rough factor of 130 when measuring behind 500 m.w.e at 18°, a factor of 800 for 1000 m.w.e at 11° and about 5000 when measuring behind 2000 m.w.e at 3° elevation. With increasing rock thickness and decreasing elevation, the importance of the background affecting the muographic measurement (the soft component) is increasing compared to the muographic signal (the ballistic muons) until it becomes dominant. As a result, the density inferred from the muographic measurement that assumes that

the measured flux is dominated by ballistic muons is increasingly biased towards lower densities when the measured rock thickness increases, until a non-physical density of the volcano is reached at some point. This is illustrated in Table 1 where we showed the effect of this background level on the muographic measurement of different thicknesses of rock. The density is inferred assuming that the background is not subtracted from a measurement that includes therefore both the expected flux of atmospheric muons transmitted through the rock and the background. In the particular case of Puy de Dôme, a reliable measurement down to an elevation of 10° (that corresponds to about 2000 m.w.e) would require decreasing the background level by a rough factor of 50.

Under the assumption that the background is isotropic and detectors similar in performance with ours are used, the background measurement given in Equations 4, 5 allows inferring the feasibility of muographic measurements in different experimental sites. Obviously, if detectors with particle identification and momentum measurement capabilities are used, the background can be further reduced.

5. Discussion and conclusion

The measurement of the flux of particles through the base of the Puy de Dôme volcano presented in this article was performed with two independent detectors, which are precursors of those foreseen by the MU-RAY and TOMUVOL collaboration. The two measurements are in agreement but are more than one order of magnitude larger than the flux of high-energy muons expected to cross the Puy de Dôme volcano at low elevation (less than 18°).

The theoretical uncertainties affecting the differential flux of atmospheric muons [*Gaisser*, 2012] were estimated to be within 30% from discrepancies between the parametrisation

used by TOMUVOL [*Chirkin*, 2004], full CORSIKA [*Heck*, 1998; *Knapp*, 2003] simulations and dedicated measurements [*Sanuki*, 2002; *Motoki*, 2003; *Haino*, 2004]. The free-sky flux measured by TOMUVOL moreover agrees within 10% with the expected flux normalisation while the angular dependency is also well reproduced. The difference in the counting rate can be therefore safely linked to a background source independent of the sought signal from high energy muons.

Though the TOMUVOL detector had no absorber, a steel plate 3 cm thick was used for the MU-RAY detector (Section 2) to suppress the so called soft component of the cosmic radiation, consisting of electrons, positrons and γ-photons. The electrons, positrons and photons are expected to shower when crossing the absorber and an electromagnetic shower can be rejected by requiring a straight track without additional energy deposits around it. The steel absorber does not stop or significantly scatter muons with kinetic energies larger than 70 MeV. The fact that the two detectors observe the same level of background hints at a main source of background that is not the soft component but rather muons with kinetic energies greater than 70 MeV.

In [*Jourde*, 2013], the DIAPHANE collaboration measured also similar background levels that they attributed to upward-going muons. Since the MU-RAY and TOMUVOL detectors do not have yet the ns time resolution that would allow them to differentiate between down-going tracks coming from the volcano and up-going tracks coming from the opposite direction (free sky), our background flux measurement could also include such a contribution. This background is necessarily decreasing with the elevation α and it could explain the behaviour of our measured background in the proximity of the horizontal

plane, below 2° elevation. Above 2°, our measured background nevertheless remains flat with the elevation angle until 8° and increases significantly with it afterwards.

A study published in [*Nishiyama*, 2014] leads to very similar results to the MU-RAY and TOMUVOL measurements presented here. That study used two emulsions-based detectors with different momentum thresholds (0.2 and 2 GeV/c) and demonstrated that low-energy particles dominate the background population. However, in that study, as well as in ours, the detectors cannot provide the necessary particle identification in order to identify unequivocally the background. One possible background source could be low energy muons that underwent large-angle scattering during their propagation in the air or in the vicinity of the detector; the background could be also due to the low energy, electromagnetic or hadronic components of the down-going atmospheric showers. The important point is however that by choosing an appropriately high momentum threshold for the detector the background level can in principle be reduced to a level low enough to allow a reliable imaging of volcanoes.

The joint measurement presented here confirms the need of further tools of background reduction to explore the interior of volcanoes over a rock thickness of half a kilometre or more. Both collaborations have already foreseen operating detectors with a higher momentum threshold and time-of-flight measurements.

Even though the 2013 data-taking campaign did not lead to an imaging of the Puy de Dôme inner structure, it is nonetheless the first measurement of the background flux behind 1000 m of rock made with two independent detectors situated farther than 1.3 km away from the volcano. It was found to correspond roughly to the expected flux of high-energy atmospheric muons at 18° elevation after crossing 600 m.w.e. Though the detection

views were South-North for the MU-RAY detector and East-West for the TOMUVOL, the measured background flux by the two detectors is consistent, hinting towards an independence with respect to the Earth magnetic field, as it would be expected in case of the soft component of the spectrum with randomised directions through scattering.

The background measurement is a first necessary step before a density measurement is envisaged. Several groups all over the world were funded over the last ten years and the number of new muographic project is steadily increasing. Quantifying the background level should help designing the experimental setups for their designed targets. As already stressed in Section 4 if the background is isotropic and detectors similar in performance with ours are used, the background measurement given in Equations 4, 5 allows inferring the feasibility of muographic measurements in different experimental sites.

Acknowledgments. The TOMUVOL collaboration acknowledges funding from the University Blaise Pascal of Clermont-Ferrand, CNRS, Région Auvergne, Conseil Général du Puy-de-Dôme. During the data taking campaign, the TOMUVOL detector was kindly hosted in a building belonging to TDF Rhône Auvergne, thanks to Luc Lecoeuvre, head of the TDF Housing Wealth department. The MU-RAY detector was graciously hosted by M. Framit in his "Gros Manaux" Inn. The LiDAR data used in this study have been provided through a collective project driven by the Centre Régional Auvergnat de l'Information Géographique (CRAIG) which has been financially supported by the Conseil Général du Puy-de-Dôme, the European Funds for Regional Development (FEDER) and the Blaise Pascal University of Clermont-Ferrand (UBP). Two of the authors of this article (L. Gailler and A. Portal) were supported by Clervolc Labex program (ANR-10-LABX-0006). This is Clervol contribution No. 138.

References

Brown, S.K., Loughlin, S.C., Sparks, R.S.J., and Vye-Brown et al., 2015. Global volcanic hazards and risk: Technical background paper for the UN-ISDR Global Assessment Report on Disaster Risk Reduction 2015, *Global Volcano Model and the International Association of Volcanology and Chemistry of the Earth's Interior*

Smith, J.G., Dehn, J., Hoblitt, R.P., LaHusen, R.G., Lowenstern, J.B., Moran, S.C., McClelland, L., McGee, K.A., Nathenson, M., Okubo, P.G., Pallister, J.S., Poland, M.P., Power, J.A., Schneider, D.J. and Sisson, T.W., 2009. Volcano monitoring. In: R. Young and L. Norby (Editors), *Geological Monitoring.* Geological Society of America, Boulder, Colorado, 273–305

Revil, A., Finizola, A., Piscitelli, S., Rizzo, E., Ricci, T., Crespy, A., Angeletti, B., Balasco, M., Barde Cabusson, S., Bennati, L., Bolve, A., Byrdina, S., Carzaniga, N., Di Gangi, F., Morin, J., Perrone, A., Rossi, M., Roulleau, E. and Suski, B., 2008. Inner structure of La Fossa di Vulcano (Vulcano Island, southern Tyrrhenian Sea, Italy) revealed by high-resolution electric resistivity tomography coupled with self-potential, temperature, and CO2 diffuse degassing measurements., *J. Geophys. Res.,* **113**, B7

Li,Y and Oldenburg, D., 1998. 3-D inversion of gravity data, *Geophysics*, **63**, 109119.

Gailler, L., Lénat, J.-F., Lambert, M., Levieux, G., Villeneuve, N., Froger, J.-L., 2009. Gravity structure of Piton de la Fournaise volcano and inferred mass transfer during the 2007 crisis, *J. Volcanol. Geotherm. Res.,* **184**, 31–48. doi:10.1016/j.jvolgeores.2009.01.024

Gailler, L. and Lénat, J.-F., 2012. Architecture of La Réunion inferred from geophysical data, *Bulletin of Volcanology,* **221-222**, 83–98. doi: 10.1016/j.jvolgeores.2012.01.015

Lees, J.M., 2007. Seismic tomography of magmatic systems, *J. Volcanol. Geotherm. Res.,* **167(1-4)**, 37-56

McGuire, W. J., 1996. Volcano instability: a review of contemporary themes, *Geological Society, London, Special Publications*, **110**(1), 1-23

Siebert, L., Glicken, H., Ui, T., 1987. Volcanic hazards from Bezymianny-and Bandai-type eruptions, *Bulletin of Volcanology,* **49(1)**, 435-459

Lopez , D. L. and Williams, S.N., Catastrophic volcano collapse: relation to hydrothermal al teration. 1993, *Science* **260**, 1794-1796

L.W. Alvarez, J.A. Anderson, F. El Bedwei, J. Burkhard, A. Fakhry, A. Girgis, A. Goneid, F. Hassan, D. Iverson, G. Lynch, Z. Miligy, A. H.Moussa, M. Sharkawi, L. Yazolino, 1970. Search for hidden chambers in the pyramids, *Science* **167**, 832

K Nagamine, M Iwasaki, K Shimomura, K Ishida, 1995. Method of probing inner-structure of geophysical substance with the horizontal cosmic-ray muons and possible application to volcanic eruption prediction, *Nucl. Instr. Meth. A,* **356**, 585-595

H. Tanaka, T, Nakano, S. Takahashi, J. Yoshida, K. Niwa, 2007. Development of an emulsion imaging system for cosmic-ray muon radiography to explore the internal structure of a volcano, Mt. Asama, *Nucl. Instr. Meth. A,* **575**, 489-497

H. K. M. Tanaka, H.Taira, T. Uchida, M. Tanaka, M. Takeo, T. Ohminato, Y. Aoki, R. Nishitama, D. Shoji, H. Tsuiji, 2010. Three dimensional computational axial tomography scan of a volcano with cosmic ray muon radiography, *J. Geophys. Res.,* **115**, B12332, doi:10.1029/2010JB007677

H.K.M. Tanaka, H. Miyajima, T. Kusagaya, A.Taketa, T. Uchida, M. Tanaka, 2011. Cosmic muon imaging of hidden seismic fault zones: Rainwater permeation into the mechan-

ical fractured zones in Itoigawa–Shizuoka Tectonic Line, Japan, *Earth and Planetary Science Letters*, Volume **306**, Issues 3-4, Pages 156-162

H.K.M. Tanaka, T. Kusagaya , H. Shinohara, 2014. Radiographic visualization of magma dynamics in an erupting volcano, *Nature Communications*, DOI: 10.1038/ncomms4381

Major, J.J., Dzurisin D., Schilling S.P., Poland M.P., 2009. Monitoring lava-dome growth during the 20042008 Mount St. Helens, Washington, eruption using oblique terrestrial photography, *Earth Planet. Sci. Lett.*, **286(1-2)**, 243–254

Vallance, J. W., Gardner, C., Scott, W. E., Iverson, R., Pierson, T., 2010. Mount St. Helens: A 30-Year Legacy of Volcanism, *EOS*, **91**, 169–170. doi:10.1029/2010EO190001

Swanson, D.A., Dzurisin, D., Holcomb, R.T., Iwatsubo, E.Y., Chadwick, W.W., Jr., Casadevall, T.J., Ewert, J.W., Heliker, C.C., 1987. Growth of the lava dome at Mount St. Helens, Washington (USA), 1981–83, in Fink, J.H., (ed.), Emplacement of silicic domes and lava flows, *Geological Society of America Special Paper*, **212**, 1–16

Nakada, S., and T. Fujii, 1993. Preliminary report on the activity at Unzen Volcano (Japan), November 1990-November 1991: Dacite lava domes and pyroclastic flows, *J. Volcanol. Geotherm. Res.,* **54(3-4)**, 319–333 doi:10.1016/0377-0273(93)90070-8.

Nakada, S., Y. Miyake, H. Sato, O. Oshima, A. Fujinawa, 1995. Endogenous growth of dacite dome at Unzen volcano (Japan), 1993–1994, *Geology*, **23(2)**, 157.

Nakada, S., H. Shimizu, K. Ohta, 89(1-4). 1-22, *J. Volcanol. Geotherm. Res.,* **1999**, Overview of the 1990–1995 eruption at Unzen Volcano. doi:10.1016/S0377-0273(98)00118-8

Calder, E. S., R. Luckett, R. S. J. Sparks, B. Voight, 2002. Mechanisms of lava dome instability and generation of rockfalls and pyroclastic flows at Soufrière Hills Volcano,

Montserrat, *Mem. Soc. LONDON*, **21**, 173190

Ryan, G. A., S. C. Loughlin, M. R. James, L. D. Jones, E. S. Calder, T. Christopher, M. H. Strutt, and G. Wadge, 2010. Growth of the lava dome and extrusion rates at Soufrière Hills Volcano, Montserrat, West Indies, 2005–2008, *Geophys. Res. Lett.,* **37**, L00E08. doi:10.1029/2009GL041477

Watts, R. ., R. A. Herd, R. S. J. Sparks, and S. R. Young, 2002. Growth patterns and emplacement of the andesitic lava dome at Soufrière Hills Volcano, Montserrat, *Geol. Soc. London, Mem.*, **21(1)**, 115152, doi:10.1144/GSL.MEM.2002.021.01.06.

Bluth, G. J. S., and W. I. Rose, 2004. Observations of eruptive activity at Santiaguito volcano, Guatemala, *J. Volcanol. Geotherm. Res.,* **136(3-4)**, 297–302. doi:10.1016/j.jvolgeores.2004.06.001.

Harris, A.J.L., Rose, W.I., Flynn, L.P., 2003. Temporal trends in lava dome extrusion at Santiaguito, 1922–2000, *Bulletin of Volcanology,* **65**, 77-89

Rose, W.I., 1972, Santiaguito Volcanic Dome, *Guatemala Geological Society of America Bulletin*, **83**, 1413–1433. doi: 10.1130/0016-7606(1972)83[1413:SVDG]2.0.CO;2

J. Marteau, D. Gibert, N. Lesparre, F. Nicollin, P. Noli, F. Giacoppo, 2012. Muons tomography applied to geosciences and volcanology, *Nucl. Instr. Meth. A,* **695**, 23-28

N. Lesparre, D. Gibert, J. Marteau, J.-C. Komorowski, F. Nicollin, O. Coutant, 2012. Density muon radiography of La Soufrière of Guadeloupe volcano: comparison with geological, electrical resistivity and gravity data, *Geophys. J Int.,* **190**, 1008-1019

F. Fehr, for the Tomuvol Collaboration, 2012. Density imaging of volcanos with atmospheric muons, *J. Phys.: Conf. Ser. 375 052019*

A. Portal, P. Labazuy, J.-F. Lénat, S. Béné, P. Boivin, E. Busato, C. Cârloganu, C. Combaret, P. Dupieux, F. Fehr, P. Gay, I. Laktineh, D. Miallier, L. Mirabito, V. Niess, and B. Vulpescu, 2013. Inner structure of the Puy de Dme volcano: cross-comparison of geophysical models (ERT, gravimetry, muon imaging), *Geosci. Instrum. Method. Data Syst.*, **2**, 47–54

F Ambrosino, A Anastasio, D Basta, L Bonechi, M Brianzi, A Bross, S Callier, A Caputo, R Ciaranfi, L Cimmino, R D'Alessandro, L D'Auria, C de La Taille, S Energico, F Garufi, F Giudicepietro, A Lauria, G Macedonio, M Martini, V Masone, C Mattone, M C Montesi, P Noli, M Orazi, G Passeggio, R Peluso, A Pla-Dalmau, L Raux, P Rubinov, G Saracino, E Scarlini, G Scarpato, G Sekhniaidze, O Starodubtsev, P Strolin, A Taketa, H K M Tanaka, A Vanzanella, L Viliani *et al.*, 2014. The MU-RAY project: detector technology and first data from Mt. Vesuvius, *JINST,* **9**, C02029

A. Anastasio, F. Ambrosino, D. Basta, L. Bonechi, M. Brianzi, A. Bross, S. Callier, A. Caputo, R. Ciaranfi, L. Cimmino, R. D'Alessandro, L. D'Auria, C. de La Taille, S. Energico, F. Garufi, F. Giudicepietro, A. Lauria, G. Macedonio, M. Martini, V. Masone, C. Mattone *et al.*, 2013. The MU-RAY detector for muon radiography of volcanoes, *Nucl. Instr. Meth. A,* **732**, 423-426.

A. Anastasio, F. Ambrosino, D. Basta, L. Bonechi, M. Brianzi, A. Bross, S. Callier, F. Cassese, G. Castellini, R. Ciaranfi, L. Cimmino, R. D'Alessandro, B. De Fazio, C. de La Taille, F. Garufi, G. Iacobucci, M. Martini, V. Masone, C. Mattone, S. Miyamoto, M.C. Montesi *et al.*, 2013. The MU-RAY experiment. An application of SiPM technology to the understanding of volcanic phenomena, *Nucl. Instr. Meth. A,* **718**, 134

G. Ambrosi, F. Ambrosino, R. Battiston, A. Bross, S. Callier, F. Cassese, G. Castellini, R. Ciaranfi, F. Cozzolino, R. DAlessandro, C. de La Taille, G. Iacobucci, A. Marotta, V. Masone, M. Martini, R. Nishiyama, P. Noli, M. Orazi, L. Parascandolo, P. Parascandolo, G. Passeggio *et al.*,2011. The MU-RAY project: Volcano radiography with cosmic-ray muons, *Nucl. Instr. Meth. A,* **628**, 120

C. Cârloganu, V. Niess, S. Béné, E. Busato, P. Dupieux, F. Fehr, P. Gay, D. Miallier, B. Vulpescu, P. Boivin, C. Combaret, P. Labazuy, I. Laktineh, J.-F. Lénat, L. Mirabito, A. Portal, 2013. Towards a muon radiography of the Puy de Dôme, *Geosci. Instrum. Method. Data Syst.*, **2**, 55–60

Boivin P., Thouret J.C., 2013. The volcanic Chaîne des Puys: A unique collection of simple and compound monogenetic edifices. In *Landscapes and Landforms of France* (Fort M. and André M.F., eds), Springer, Heidelberg, 9, 81–91

Camus, G., 1975. La Chaîne des Puys. Etude structurale et volcanologique, *PhD thesis* no **56**, Clermont II, 322 p

Miallier, D., Boivin P., Deniel C., Gourgaud A., Lanos P., Sforna M., and Pilleyre T., 2010, The ultimate summit eruption of Puy de Dôme volcano (Chaîne des Puys, French Massif Central) about 10,700 years ago, *Comptes Rendus Geosci.*, **342(11)**, 847–854, doi:10.1016/j.crte.2010.09.004

Boivin P., Besson J.C., Briot D., Camus G., de Goër de Herve A., Gourgaud A., Labazuy P., Langlois E., de Larouzière F.D., Livet M., Mergoil J., Miallier D., Morel J.M., Vernet G., Vincent P., 2009 Volcanologie de la Chane des Puys, *Parc Naturel Rgional de la Chane des Puys (Edit.)*, 196p

S. Okubo, H.K.M. Tanaka, 2012. Imaging the density profile of a volcano interior with cosmic-ray muon radiography combined with classical gravimetry, *Meas. Sci. Technol.*, **23** 042001, Doi:10.1088/0957-0233/23/4/042001

S. Matsuno, F. Kajino, Y. Kawashima, T. Kitamura, K. Mitsui, Y. Muraki, Y. Ohashi, A. Okada, T. Suda, Y. Minorikawa, K. Kobayakawa, Y. Kamiya, I. Nakamura, and T. Takahashi, 1984. Cosmic-ray muon spectrum up to 20 TeV at 89° zenith angle, *Phys. Rev. D,* **29**, 1

K.A. Olive et al. (Particle Data Group), 2014. The Review of Particle Physics, *Chin. Phys. C*, **38**, 090001 and http://pdg.lbl.gov/2014/AtomicNuclearProperties/index.html

S. Agostinelli et al (Geant 4 collaboration), 2003. Geant4—a simulation toolkit, *Nucl. Instr. Meth. A,* **506**, 250–303

D. Chirkin, 2004. Fluxes of Atmospheric Leptons at 600 GeV - 60 TeV, arxiv:hep-ph/0407078

D.E. Groom, N.V. Mokhov, and S.I. Striganov, 2001. Muon stopping power and range tables 10 MeV100 TeV, *Atomic Data and Nuclear Data Tables* **78**, 183–356

A. Pla-Dalmau, A. D. Bross, K. L. Mellot, FERMILAB-Conf-99/095

A. Piazza, M. Boscardin, G.-F. Dalla Betta, A. Del Guerra, M. Melchiorri, C. Piemonte, A. Tarolli, N. Zorzi, 2010. Characterization and simulation of different SiPM structures produced at FBK, *Nucl. Instr. Meth. A,* **617**, 417–419

G. Punzi, Phystat 2003: Sensitivity of Searches for New Signals and Its Optimization, Scuola Normale Superiore and INFN, Pisa, Italy

M Bedjidian, K Belkadhi, V Boudry, C Combaret, D Decotigny, E Cortina Gil, C de la Taille, R Dellanegra, V A Gapienko, G Grenier, C Jauffret, R Kieffer, M -C Fouz, R

Han, I Laktineh, N Lumb, K Manai, S Mannai, H Mathez, L Mirabito, J Puerta Pelayo, M Ruan, F Schirra, N Seguin-Moreau, W Tromeur, M Tytgat, M Vander Donckt and N Zaganidis, 2011. Performance of Glass Resistive Plate Chambers for a high-granularity semi-digital calorimeter, *JINST,* **6**, P02001, doi:10.1088/1748-0221/6/02/P02001

T. Behnke (ed.), "The International Linear Collider Technical Design Report - Volume 4: Detectors" , Jun 26, 2013. 384 pp, CERN-ATS-2013-037, arXiv:1306.6329

N. Seguin-Moreau, S. Callier, F. Dulucq, C. De La Taille, G. Martin-Chassard, in "Topical Workshop on Electronics for Particle Physics (TWEPP-09)" proceedings, Sep 2009, Paris, France. Cern, pp.122-126

S. Callier, J.-B Cizel, F. Dulucq, C. de La Taille, G. Martin-Chassard, N. Seguin-Moreau 2014. ROC chips for imaging calorimetry at the International Linear Collider, *JINST,* **9**, C02022

C. Adloff, J. Blaha, M. Chefdeville, A. Dalmaz, C. Drancourt, A. Espargilire, R. Gaglione, N. Geffroy, D. Girard, J. Jacquemier, Y. Karyotakis, I. Koletsou, F. Peltier, J. Samarati, S. Tsigaridas, G. Tsipolitis, G. Vouters, 2013. Construction and test of a 1×1 m^2 Micromegas chamber for sampling hadron calorimetry at future lepton colliders, *Nucl. Instr. Meth. A,* **729**, 90101

Observatoire de Physique du Globe de Clermont Ferrand, http://wwwobs.univ-bpclermont.fr/opgc/index.php

T.K. Gaisser, 2012. Spectrum of cosmic-ray nucleons, kaon production, and the atmospheric muon charge ratio, *Astropart. Phys.,* **35**, 801–806, DOI: 10.1016/j.astropartphys.2012.02.010

D. Heck, J. Knapp, J.N. Capdevielle, G. Schatz, T. Thouw, 1998. A Monte Carlo Code to Simulate Extensive Air Showers, *Forschungszentrum Karlsruhe Report* FZKA 6019

J. Knapp, D. Heck, S.J. Sciutto, M.T. Dova, and M. Risse, 2003. Extensive Air Shower Simulations at Highest Energies, *Astropart. Phys.,* **19**, 77

T Sanuki, M Fujikawa, K Abe, K Anraku, Y Asaoka, H Fuke, S Haino, M Imori, K Izumi, T Maeno, Y Makida, N Matsui, H Matsumoto, H Matsunaga, M Motoki, J Nishimura, M Nozaki, S Orito, M Sasaki, Y Shikaze, T Sonoda, et al., 2002. Measurements of atmospheric muon spectra at mountain altitude, *Phys. Lett. B,* **541**, 234–242 Erratum-ibid. B581 (2004) 272-273 DOI: 10.1016/S0370-2693(02)02265-7

M. Motoki, T. Sanuki, S. Orito, K. Abe, K. Anraku, Y. Asaoka, M. Fujikawa, H. Fuke, S. Haino, M. Imori, K. Izumi, T. Maeno, Y. Makida, N. Matsui, H. Matsumoto, H. Matsunaga, J. Mitchell, T. Mitsui, A. Moiseev, J. Nishimura, M. Nozaki, J. Ormes, T. Saeki, M. Sasaki, E.S. Seo, Y. Shikaze, T. Sonoda, R. Streitmatter, J. Suzuki, K. Tanaka, I. Ueda, J.Z. Wang, N. Yajima, T. Yamagami, A. Yamamoto, Y. Yamamoto, K. Yamato, T. Yoshida, K. Yoshimura, 2003. Precise measurements of atmospheric muon fluxes with the BESS spectrometer, *Astropart. Phys.,* **19**, 113-126 DOI: 10.1016/S0927-6505(02)00195-0

S. Haino, T. Sanuki, K. Abe, K. Anraku, Y. Asaoka, H. Fuke, M. Imori, A. Itasaki, T. Maeno, Y. Makida, S. Matsuda, N. Matsui, H. Matsumoto, J.W. Mitchell, A.A. Moiseev, J. Nishimura, M. Nozaki, S. Orito, J.F. Ormes, M. Sasaki, E.S. Seo, Y. Shikaze, R.E. Streitmatter, J. Suzuki, Y. Takasugi, K. Tanaka, K. Tanizaki, T. Yamagami, A. Yamamoto, Y. Yamamoto, K. Yamato, T. Yoshida, K. Yoshimura, 2004. Measurements of primary and atmospheric cosmic-ray spectra with the BESS-TeV spectrometer, *Phys.*

Lett. B, **594**, 35.

K. Jourde, D. Gibert, J. Marteau, J. De Bremond DArs, S. Gardien, C. Girerd, J.-C. Ianigro, D. Carbone, 2013. Experimental detection of upward going cosmic particles and consequences for correction of density radiography of volcanoes, *Geophys. Res. Lett.,* **40**, 6334-6339 doi:10.1002/2013GL058357

R. Nishiyama, S. Miyamoto, N. Naganawa, 2014. Experimental study of source of background noise in muon radiography using emulsion film detectors, *Geosci. Instrum. Method. Data Syst.*, **3**, 29-39 doi:10.5194/gi-3-29-2014

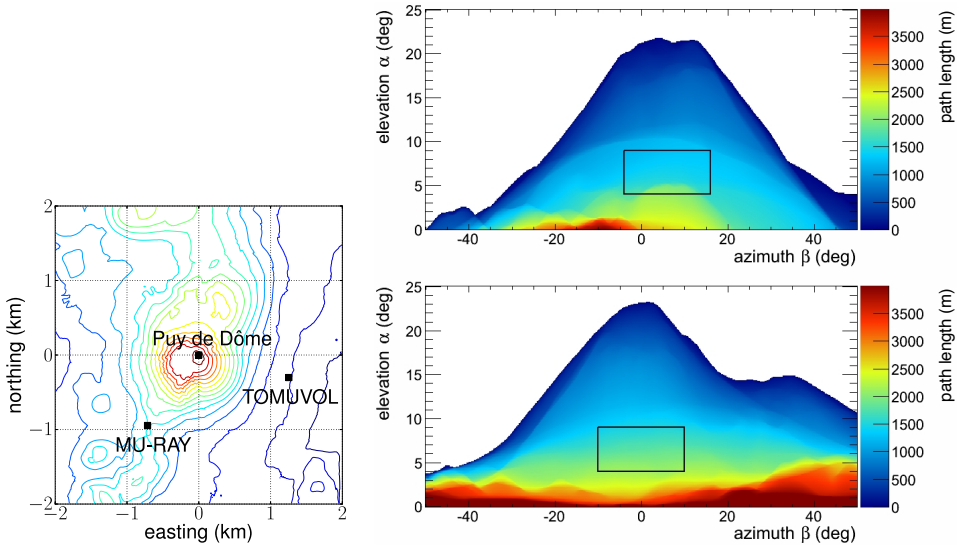

Figure 1. *Top:* the deployment sites for the MU-RAY and TOMUVOL detectors on the flank of the Puy de Dôme volcano. The level curves go from 880 m to 1440 m, in 40 m steps. The path length traveled by the atmospheric muons through the volcano before reaching the MU-RAY (*middle plot*) and TOMUVOL (*bottom plot*) detectors, as a function of the elevation angle α and azimuth β. The control regions, defined by $\alpha \in (4°, 9°)$ and $\beta \in (-4°, 16°)$ (MU-RAY) or $\mid \beta \mid \leq 10°$ (TOMUVOL), are indicated by the black rectangles.

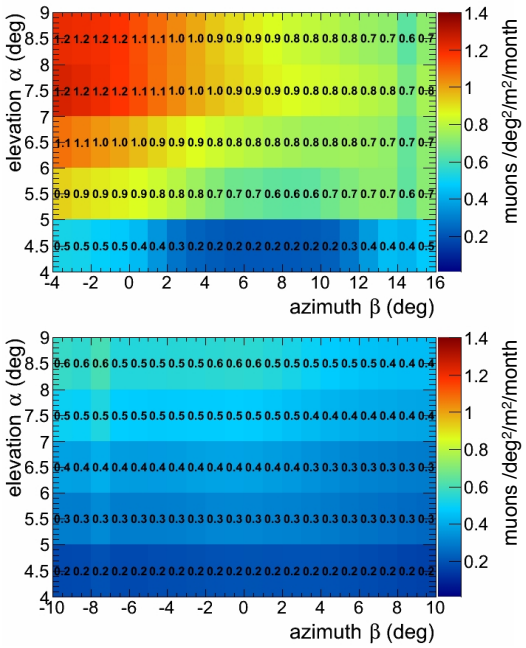

Figure 2. Expected number of muons crossing the control regions in a month and measurable with a 1 m^3, ideal detector, as a function of the elevation angle α and azimuth β. The detector is supposed to be fully efficient, with a detection threshold of 100 MeV and is located either at the MU-RAY (*top*) or TOMUVOL (*bottom*) deployment sites. The volcano density is assumed to be 1.66 g/cm^3 and uniform.

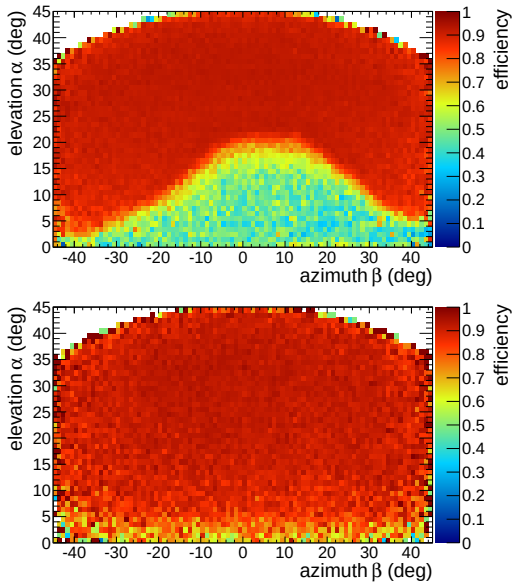

Figure 3. MU-RAY selection efficiency for the tracks pointing towards Puy de Dôme (*top*) and in the opposite direction (*bottom*) as a function of the elevation angle α and azimuth β.

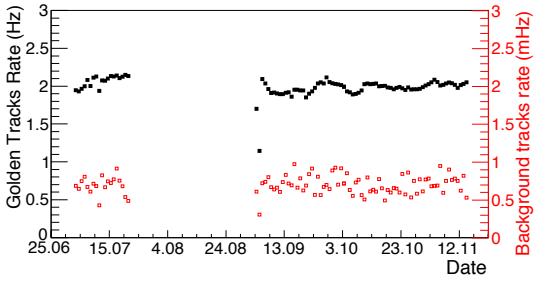

Figure 4. Rate of "golden tracks" (black squares, in Hz) and background tracks (open red squares, in mHz), registered with the MU-RAY detector. The rates are corrected for the acquisition dead time.

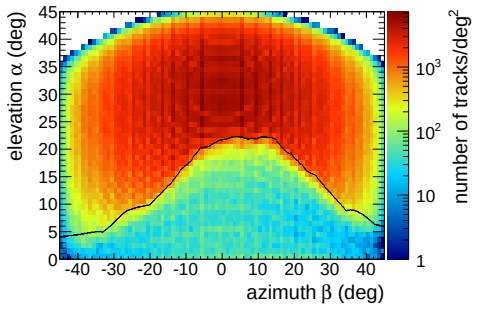

Figure 5. MU-RAY golden tracks towards Puy de Dôme as a function of the elevation angle α and azimuth β. The topographical shape of the Puy de Dôme is superimposed in black.

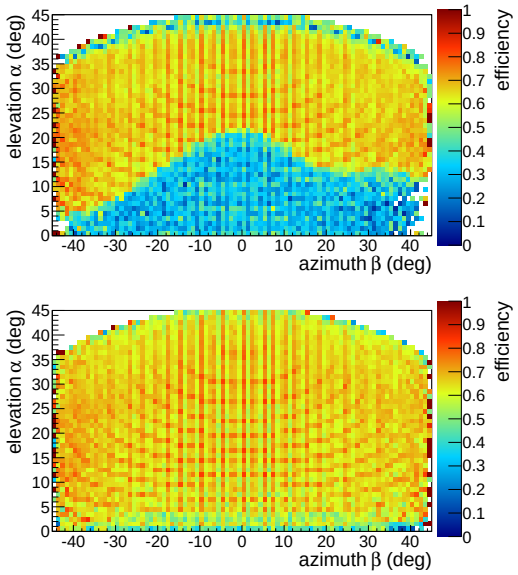

Figure 6. Percentage of isolated tracks with $\chi^2/n.d.f \leq 0.8$ in the original sample of reconstructed tracks as a function of the elevation α and azimuth β. *Top* : sample of tracks pointing towards Puy de Dôme; *bottom* : sample of tracks pointing in the opposite direction of Puy de Dôme.

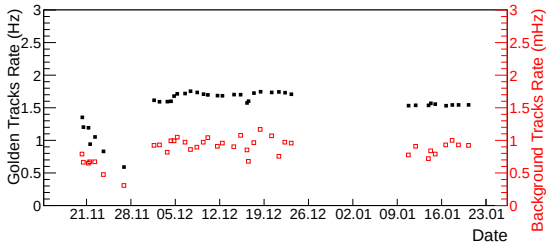

Figure 7. Rates of "golden tracks" recorded with the TOMUVOL detector (black squares, in Hz) and background tracks (open red squares, in mHz). The rates are corrected for the acquisition dead time. During the runs before November 28th the detector working conditions (mainly high voltage applied on the GRPCs) were scanned in order to define an optimal working point.

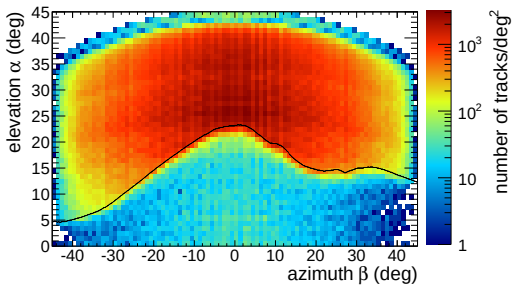

Figure 8. Golden tracks recorded by the TOMUVOL detector and pointing towards the Puy de Dôme as a function of the elevation angle α and azimuth β.

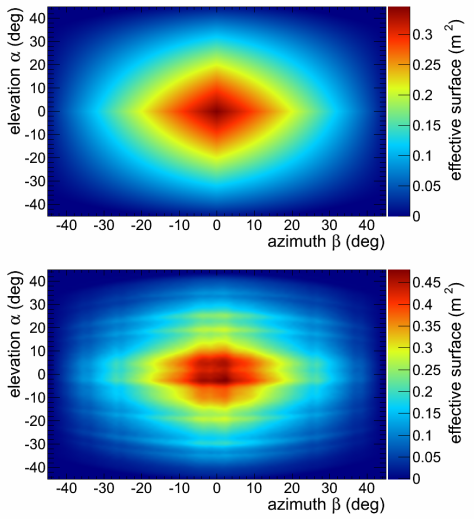

Figure 9. Effective surface as a function of the elevation angle α and azimuth β for MU-RAY (*top*) and TOMUVOL (*bottom*) detectors.

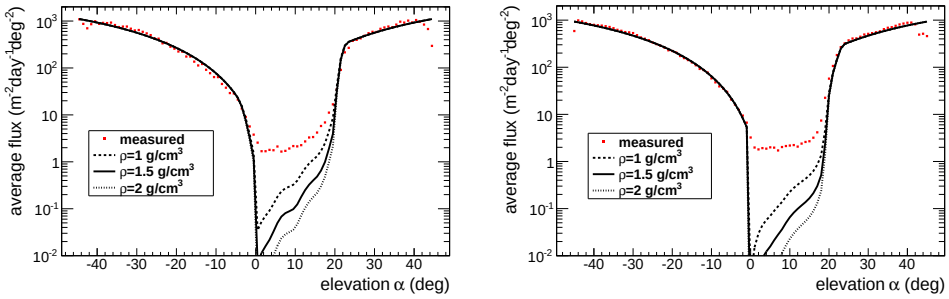

Figure 10. Muon flux as a function of the elevation α, as measured with the MU-RAY (*top*) and TOMUVOL (*bottom*) detectors.

Table 1. Transmitted flux of ballistic atmospheric-muons behind different rock thicknesses and the inverted density through a muographic measurement affected by a background flux of 1.94 $m^{-2}day^{-1}deg^{-2}$ (the quadratic mean of the MU-RAY and TOMUVOL measurements given in Equations 4, 5).

Integrated density (true, mwe)	elevation angle (deg)	transmitted flux ($m^{-2}day^{-1}deg^{-2}$)	integrated density (measured, m.w.e)	bias %
500	18	3.18	389.7	-22
1000	11	0.83	539.6	-46
2000	3	0.19	498.3	-75